PTEP

Prog. Theor. Exp. Phys. **2012**, 01A306 (23 pages)
DOI: 10.1093/ptep/pts018

Formation and radiative feedback of first objects and first galaxies

Masayuki Umemura[1,*], Hajime Susa[2], Kenji Hasegawa[1], Tamon Suwa[3], and Benoit Semelin[4,5]

[1]*Center for Computational Sciences, University of Tsukuba, Tsukuba, Ibaraki 305-8577, Japan*
[2]*Department of Physics, Konan University, Okamoto, Kobe 658-8501, Japan*
[3]*Fujitsu Limited, Kawasaki 211-8588, Japan*
[4]*LERMA, Observatoire de Paris, CNRS, 61 Av. de l' Observatoire, 75014 Paris, France*
[5]*Université Pierre et Marie Curie, 4 place Jussieu, 75005 Paris, France*
*E-mail: umemura@ccs.tsukuba.ac.jp

Received May 1, 2012; Accepted July 12, 2012; Published October 9, 2012

Firstly, the formation of first objects driven by dark matter is revisited by high-resolution hydrodynamic simulations. It is revealed that dark matter halos of $\sim 10^4\ M_\odot$ can produce first luminous objects with the aid of dark matter cusps. Therefore, the mass of first objects is smaller by roughly two orders of magnitude than in the previous prediction. This implies that the number of Population III stars formed in the early universe could be significantly larger than hitherto thought. Secondly, feedback by photo-ionization and photo-dissociation photons in the first objects is explored with radiation hydrodynamic simulations, and it is demonstrated that multiple stars can form in a $10^5\ M_\odot$ halo. Thirdly, the fragmentation of an accretion disk around a primordial protostar is explored with photo-dissociation feedback. As a result, it is found that photo-dissociation can reduce the mass accretion rate onto protostars. Also, protostars as small as $0.8\ M_\odot$ may be ejected and evolve while keeping their mass, which might be detected as the "real first stars" in the Galactic halo. Finally, state-of-the-art radiation hydrodynamic simulations are performed to investigate the internal ionization of first galaxies and the escape of ionizing photons. We find that UV feedback by forming massive stars enhances the escape fraction even in a halo as massive as $> 6 \times 10^9\ M_\odot$, while it reduces the star formation rate significantly. This may have a momentous impact on cosmic reionization.

1. Introduction

First-generation objects and galaxies in the early universe are of great significance as progenitors of present-day galaxies, sources for cosmic reionization, the origin of heavy elements, and generators of seed black holes for supermassive black holes inhabiting galactic centers.

The formation of first-generation objects has been explored by many authors. Originally, the minimum halo mass that can undergo gravitational instability was estimated to be from $5 \times 10^4\ M_\odot$ at redshift $z \sim 100$ to $5 \times 10^7\ M_\odot$ at $z \sim 10$ from analytic arguments [1], where $M_\odot$ is the solar mass. Later on, 3D hydrodynamic simulations [2] showed the minimum mass to be from $10^5\ M_\odot$ at redshift $z \sim 100$ to $10^6\ M_\odot$ at $z \sim 10$. Since then, full cosmological hydrodynamic simulations have been performed to show that the minimum mass is a weak function of redshift, which is $\sim 7 \times 10^5\ M_\odot$ in halo mass and $\sim 10^5\ M_\odot$ in baryonic mass [3]. As for the secondary collapse of first objects under the influence of preforming stars, radiative feedback through photo-ionization of hydrogen, photo-dissociation of hydrogen molecules, and a combination of the two is important. This issue has been

explored by radiation hydrodynamics, where hydrodynamic simulations are coupled with radiative transfer calculations [4–6].

Also, in the last decade, the mass of Population III (Pop III) stars has been studied extensively. It has been shown that first stars are likely to be as massive as 100–1000 $M_\odot$ [10–13]. On the other hand, if the collapse of a first object into a flat disk is considered, first stars may form in a bimodal fashion with peaks of $\sim$1 $M_\odot$ and several 100 $M_\odot$ [14]. Besides, the mass of massive Pop III stars could be reduced to 20–40 $M_\odot$ by cosmic variance [15], external feedback [6], or internal feedback [16]. These works focused on the runaway collapse phase of first objects. Very recently it has been shown that, in the accretion phase, the disk around a first protostar can fragment into smaller pieces, eventually allowing the formation of less massive stars down to $\sim$1 $M_\odot$ or subsolar values [18–20]. Even in such a fragmented primordial disk, stars that form earlier can make a significant impact through radiation hydrodynamic feedback on subsequent star formation.

The first-generation and second-generation stars are assembled into first galaxies. Ultraviolet (UV) radiation from massive stars in first galaxies can play an important role not only in the following star formation history but also as the source for cosmic reionization. The escape of ionizing photons from first galaxies is regulated by the ionization of interstellar medium. This issue should also be investigated with radiation hydrodynamics.

In this paper, we present recent high-resolution hydrodynamic simulations on first objects and radiation hydrodynamic simulations on the radiative feedback in these objects. Also, the fragmentation of an accretion disk around a first protostar is explored with photo-dissociation feedback, and radiation hydrodynamic simulations are performed to investigate the internal ionization of first galaxies and the escape of ionizing photons. In Sect. 2, a dedicated simulator for radiation hydrodynamics, which has been developed for the present purpose, is described. In Sect. 3, the collapse of first objects driven by dark matter cusps is explored. The radiation hydrodynamic feedback there is studied in Sect. 4. In Sect. 5, the fragmentation of a first protostellar disk and radiative feedback by photo-dissociation photons are explored with radiation hydrodynamic simulations. In Sect. 6, the photo-ionization of first galaxies and the escape fraction of ionizing photons are analyzed based on radiation hydrodynamic simulations. Section 7 is devoted to the summary.

2. *FIRST* project

In order to explore extensively the hydrodynamic and radiation hydrodynamic processes during the formation of first objects and first galaxies, we have built up a dedicated simulator called *FIRST*, on the basis of the *FIRST* project [22].

The *FIRST* project was initiated by a Specially Promoted Research in Grants-in-Aid for Scientific Research by MEXT over four years (2004–2007) with a budget of JPY 329.5 million (US $4.1 million), and has been continued with a Grant-in-Aid for Scientific Research (S) (2008–2012) by JSPS with a budget of JPY 73.1 million (US $0.9 million). In this project, we constructed a new hybrid simulator, *FIRST* (Fusional Integrator for Radiation-hydrodynamic Systems in Tsukuba University). The *FIRST* simulator is a large-scale hybrid PC cluster, where each node possesses a newly-developed board for gravity calculations, Blade-GRAPE. The Blade-GRAPE is composed of four GRAPE-6A chips [21]. The theoretical peak performance of one Blade-GRAPE board is 136.8 Gflops. Each board has 16 MB of memory and can treat 260 000 particles simultaneously. The Blade-GRAPE is directly connected via PCI-X bus. Each server PC is equipped with a multi-port Gigabit Ethernet NIC that is connected to a special interconnection network using commodity Ethernet switches.

First 256

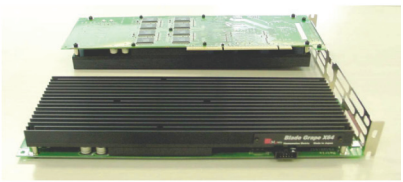

Blade-GRAPE X64

Fig. 1. The *FIRST* simulator composed of 256 nodes (*left*) and an accelerator, Blade-GRAPE, for gravity calculations, which is embedded in each node (*right*).

The first version of Blade-GRAPE works with 32 bit and 33 MHz (PCI). Then, it was improved to a 64 bit and 100 MHz version (PCI-X), Blade-GRAPE X64. Using Blade-GRAPEs, we have constructed a hybrid PC cluster system composed of 256 nodes, the *FIRST* simulator (Fig. 1). The system possesses 224 Blade-GRAPE X64 boards and 16 Blade-GRAPE boards. The host PC cluster node is a 2U-size server PC (HP ProLiant DL380 G4) that has dual Xeon processors in an SMP configuration. As a result, the total performance of the *FIRST* simulator is 36.1 Tflops, where the host PC cluster is 3.1 Tflops and the Blade-GRAPEs are 33 Tflops. All nodes are connected uniformly to each other via a multi-port Gbit ethernet interconnect switch. The total memory of the *FIRST* simulator is 1.6 TB. Also, the Gfarm Grid file system (http://datafarm.apgrid.org/index.en.html) is installed. With Gfarm, a total storage of 89.2 TB is available as a seamless file server.

In this paper, we present hydrodynamic and radiation hydrodynamic simulations on the formation of first objects and first galaxies with the *FIRST* simulator.

3. Collapse of first objects by dark matter cusps

The efficiency of the formation of first objects is extremely significant because they are responsible for the reionization history in the universe and cosmic chemical enrichment. Yoshida et al. [3] have shown that the minimum mass is a weak function of redshifts, which is $\sim 7 \times 10^5\, M_\odot$ in halo mass and $\sim 10^5\, M_\odot$ in baryonic mass. The minimum mass is basically determined by the thermal instability via hydrogen molecules (H_2). H_2 molecules form in non-equilibrium processes with the catalysis of free electrons as

$$\begin{aligned} e^- + \mathrm{H} &\rightarrow \mathrm{H}^- + h\nu \\ \mathrm{H}^- + \mathrm{H} &\rightarrow \mathrm{H}_2 + e^-. \end{aligned} \tag{3.1}$$

If the temperature exceeds 10^3 K around the number density of 1 cm^{-3}, the formation rate of H_2 molecules is increased, resulting in the H_2 abundance of $y_{H_2} \sim 10^{-3}$. Then, thermal instability occurs and the temperature decreases down to $\sim$300 K with increasing density. Then, the runaway collapse of the cloud proceeds through gravitational instability. The simulations by Yoshida et al. demonstrated that, for a halo mass below $7 \times 10^5\, M_\odot$, the virial temperature cannot be increased to $\sim 10^3$ K, and therefore the thermal instability by H_2 cooling does not occur. The mass resolution of their simulations is $\approx 30\, M_\odot$. Recently, Umemura et al. [23,24] have found by simulations with

Table 1. Models and mass resolution.

Model	$(N_{\rm DM}, N_{\rm b})$	$(m_{\rm DM}, m_{\rm b})$ $[M_\odot]$
R64	$(64^3, 64^3)$	(24.1, 5.08)
R128	$(128^3, 128^3)$	(3.01, 0.64)
R256	$(256^3, 256^3)$	(0.38, 0.079)
R512	$(512^3, 512^3)$	(0.047, 0.0099)

higer mass resolution that significantly smaller mass halos allow the collapse of primodial clouds via the H_2 cooling instability. The major difference from previous simulations is the fact that the mass resolution is much higher and remains unchanged throughout the simulations, in contrast to the adaptive change of resolutions in previous works. Umemura et al. argued that the runaway in a smaller dark halo could be induced by the cusp of the dark halo. In other words, the resolved cusp potential can raise the central temperature of the cloud up to $\sim 10^3$ K and leads to thermal instability via H_2. In this paper, to verify this conjecture, we compare the numerical results with different mass resolutions, and analyze the dark matter cusp-induced collapse.

3.1. Set-up of simulations

The formation of first objects from primordial gas is driven by dark matter fluctuations and cooling by H_2 molecules. In order to investigate the dependence on the dark matter potential, we perform high-resolution cosmological hydrodynamic simulations in a standard ΛCDM cosmology with the parameters $(\Omega_\Lambda, \Omega_{\rm m}, \Omega_{\rm b}, h) = (0.72, 0.24, 0.042, 0.73)$. First, we perform pure N-body simulations for dark matter in a larger box with a commoving linear scale of 1 Mpc and find the highest density domain of $(60\,{\rm kpc})^3$. For this domain, the evolution of density fluctuations is recalculated including baryons from the recombination epoch ($z = 10^3$). We use a particle–particle–particle–mesh (P^3M) scheme for gravity force calculations, and the baryonic component is treated with the smoothed particle hydrodynamics (SPH) method. Radiative heating/cooling and chemical reactions for e^-, H, H^+, H^-, H_2, and H_2^+ are included, where helium and deuterium reactions are dismissed. The direct part of self-gravity is calculated with Blade-GRAPE in the *FIRST* simulator. The simulations do not use any zoom-in technique, but the mass resolution is uniform over the whole computational domain and throughout the evolution. The system mass is $6.3 \times 10^6\ M_\odot$ in dark matter and $1.6 \times 10^6\ M_\odot$ in baryonic matter. The models with different resolutions are summarized in Table 1.

3.2. Growth of dark matter cusps

A dark matter fluctuation in the computational domain enters a non-linear stage around $z = 30$. In the course of the non-linear evolution, dark matter forms a virialized halo, and simultaneously a central cusp develops. The growth of the cusp depends on the mass resolution. In Fig. 2, the mass distributions are shown for different mass resolution simulations. In model R256, the cusp intrudes to radii of $\sim$1 pc. The density distribution is well fitted by $\rho \propto r^{-1.6}$. In the low or intermediate resolution case (model R64 or R128), the cusp is smoothed out in the innermost regions. The dark matter density profile with a cusp is often expressed by

$$\rho(r) = \rho_s (r/r_s)^{-a} [1 + (r/r_s)^b]^{(3-a)/b}, \tag{3.2}$$

where r_s is a characteristic inner radius and ρ_s is the corresponding inner density. In the NFW profile [25], $(a, b) = (1, 1)$ and the mass enclosed within r is $M(r) = 4\pi r_s^3 \ln[1 + (r/r_s)] - (r/r_s)/$

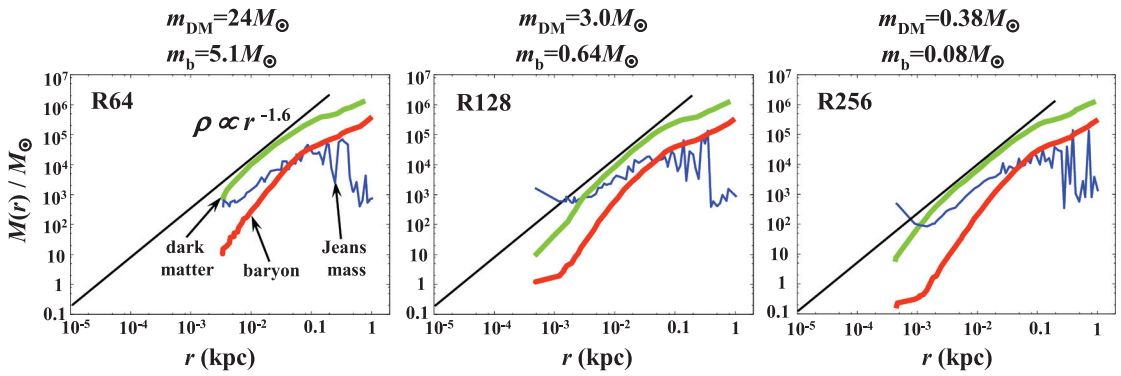

Fig. 2. The cumulative mass of dark matter and baryons is shown against the radius at $z = 16$ for different mass resolution simulations. The left panel shows model R64, the middle panel model R128, and the right panel model R256. A straight line shows the mass corresponding to the density distribution of $\rho \propto r^{-1.6}$. The Jeans mass including dark matter that is defined by (3.4) is also shown.

$[1 + (r/r_s)]$, or, in the Moore's profile, [27] $(a, b) = (1.5, 1.5)$ and the mass is

$$M(r) = (8\pi/3)\rho_s r_s^3 \ln[1 + (r/r_s)^{1.5}]. \tag{3.3}$$

The pure N-body simulations of dark matter hitherto performed have shown that the cusp profiles are between the NFW profile and the Moore's one. [25–27,29,30] The profiles of cusps ($\rho \propto r^{-1.6}$) in the present simulations are close to the Moore's profile, although the preset results are slightly steeper. (This may be the effect of dissipation of the baryonic component.) For a virialized halo with $\approx 10^4\, M_\odot$, the cusp mass is $\approx 10^3\, M_\odot$ if the concentration parameter is $c \equiv r_{\rm vir}/r_s \approx 10$ with the virial radius $r_{\rm vir}$. If the mass of dark matter particles is higher than $M_\odot$, a cusp with $\approx 10^3\, M_\odot$ is made of fewer than several hundred particles. The two-body relaxation proceeds in a timescale of $0.1 N t_{\rm dyn}/\ln N$, where N is the number of particles and $t_{\rm dyn}$ is the dynamical time. If $N < 10^3$, the two-body relaxation timescale is less than $8t_{\rm dyn}$. Thus, the dark matter cusp is inevitably erased by the two-body relaxation. Actually, in model R64 ($m_{DM} = 24.1\, M_\odot$) or R128 ($m_{DM} = 3.01\, M_\odot$), the mass distribution decreases steeply toward the center. This meams that the central cusps are smoothed out by the two-body relaxation. On the other hand, in model R256 ($m_{DM} = 0.38\, M_\odot$), a cusp grows down to $\sim$1 pc. Consequently, the central dark matter potential becomes deeper.

In Fig. 2, we also show the Jeans mass defined by

$$M_J(r) \equiv \rho_b \left(\frac{c_s^2}{G\bar{\rho}_{tot}}\right)^{3/2} = \rho_b \left(\frac{4\pi r^3 c_s^2}{3G[M_{\rm DM}(r) + M_{\rm b}(r)]}\right)^{3/2}, \tag{3.4}$$

where c_s is the local sound velocity, and $M_{\rm DM}$ and $M_{\rm b}$ are the cumulative mass of dark matter and baryons, respectively. As can be clearly seen, for higher mass resolution the Jeans mass is reduced in innermost regions owing to the dark matter cusp. The central dark matter potential is responsible for the temperature, which is directly related to the thermal instability by H_2 molecules.

3.3. Thermal instability induced by a dark matter cusp

In Fig. 3, the evolution of baryonic density fluctuations induced by dark matter is shown from $z = 90$ to $z = 17$ for model R256. If the dark matter particle mass is less than $1\, M_\odot$, the cusp with a density profile of $r^{-1.6}$ is resolved down to $<10^3\, M_\odot$. In contrast to previous work, multiple peaks can collapse induced by dark matter cusps. In Fig. 4, the density distributions at $z = 12$ are compared between different resolutions. If the dark matter resolution is lower than $m_{\rm DM} = 10\, M_\odot$, the cusp

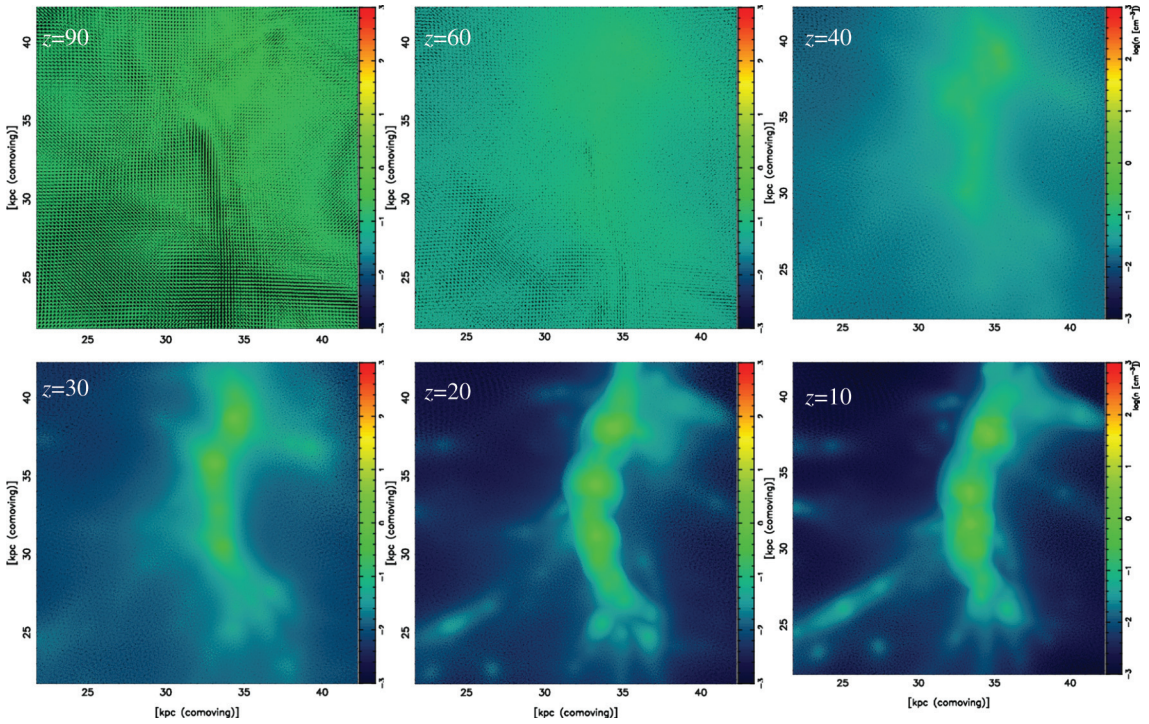

Fig. 3. Evolution of baryonic density fluctuations from $z = 90$ to $z = 17$ for model R256. Colors show the density according to the legend of the colored bar.

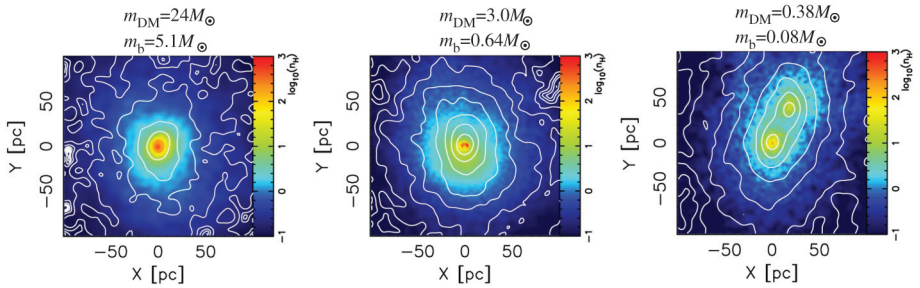

Fig. 4. Spatial density distributions of baryons and dark matter at $z = 12$ are shown for different resolution simulations. The left panel shows model R64, the middle panel model R128, and the right panel model R256. Colors shows baryonic density according to the attached legend, and contours show the levels of dark matter density.

cannot be resolved sufficiently in a halo of $10^4\,M_\odot$, and small-scale peaks readily merge into a larger peak, and consequently only one baryon condensation collapses within a halo. This evolution is basically equivalent to the previous work. But, in model R256 ($m_{\rm DM} = 0.38\,M_\odot$), a double peak forms, where the mass of each peak is $\approx 10^4\,M_\odot$ in dark matter and $\approx 10^3\,M_\odot$ in baryons. The separation of the peaks is roughly 60 pc. Unless they undergo thermal instability, the collapse of each peak bounces and the peaks may eventually merge into one larger peak. Using Eq. (3.3), the baryonic gas temperature in the cusp region can be evaluated as

$$T_{\rm cusp} = \frac{GM(r)}{r} \cdot \frac{\mu m_p}{k_B} \simeq 1040\,{\rm K} \left(\frac{\rho_s}{1.6 \times 10^{-22}\,{\rm gcm}^{-3}}\right) \left(\frac{r_s}{10\,{\rm pc}}\right)^3 \left(\frac{r}{10\,{\rm pc}}\right)^{-1}, \tag{3.5}$$

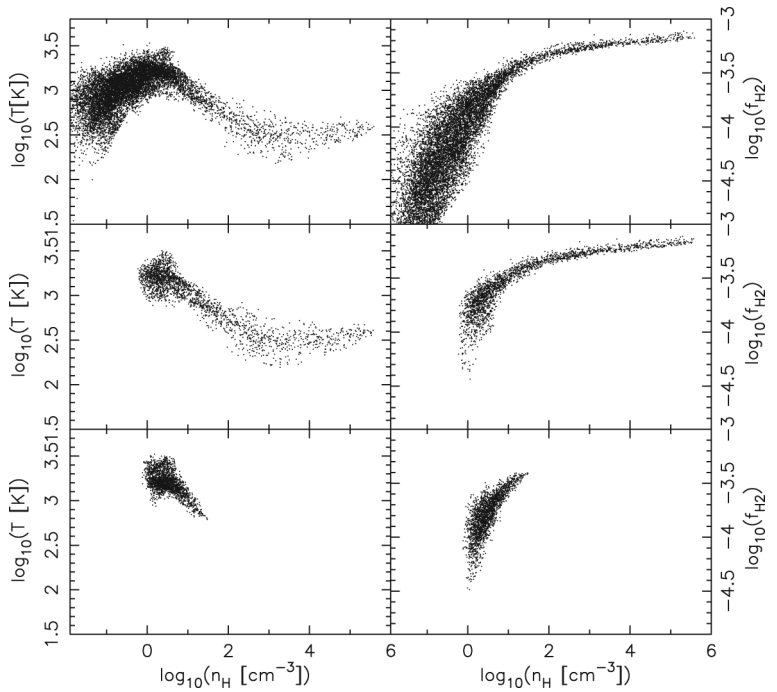

Fig. 5. Temperature (*left*) and H_2 fractions (*right*) versus baryon number density in model R256 are shown for all particles (*top panels*), the particles in the highest peak (*middle panels*), and the particles in the second highest peak (*bottom panels*).

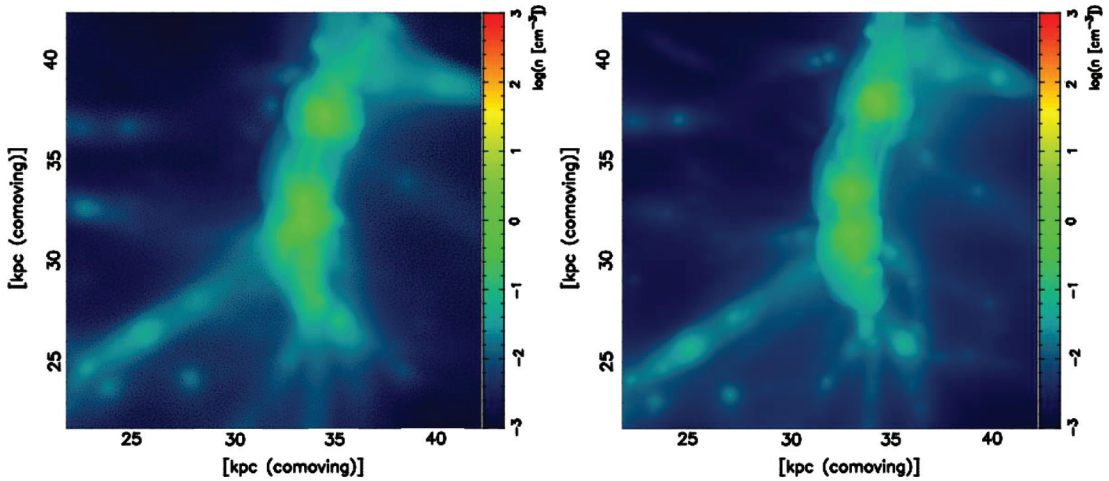

Fig. 6. Baryonic density distributions are compared at $z = 15.6$ between model R256 (*left*) and R512 (*right*). Colors shows baryonic density according to the attached legend.

where μ is the mean molecular weight, m_p is the proton mass, and k_B is the Boltzmann constant. Thus, if the cusp potential is resolved, the temperature can be raised up to $\gtrsim 10^3$ K, and then thermal instability through H_2 cooling can occur. In Fig. 5, the temperature and H_2 fractions in model R256 are shown versus baryon number density. The top panels present those for all particles, the middle panels the particles in the highest peak, and the bottom panels the particles in the 2nd highest peak. This figure shows that H_2 fractions reach a level of several 10^{-4} around a density of $n_{\rm H} \sim 1\,{\rm cm}^{-3}$ in the first and 2nd peaks. Then, the temperature decreases via thermal instability in both peaks. What is important is that, although the halo mass of peaks is of the order of $\sim 10^4\,M_\odot$, the temperature reaches

Table 2. Properties of Pop III stars.

Mass	$T_{\rm eff}$ (K)[a)]	$\dot{N}_{\rm ion}$ (s^{-1})[b)]	$L_{\rm LW}$(erg/s)[c)]
120 $M_\odot$	9.57×10^4	1.069×10^{50}	5.34×10^{23}
80 $M_\odot$	9.33×10^4	5.938×10^{49}	3.05×10^{23}
40 $M_\odot$	7.94×10^4	1.873×10^{49}	1.17×10^{23}
25 $M_\odot$	7.08×10^4	5.446×10^{48}	3.94×10^{22}

a) Effective temperature
b) Number of ionizing photons emitted per second
c) Luminosity of photo-dissociation radiation at the Lyman–Werner (LW) band

over $\sim 10^3$ K around $n_{\rm H} \approx 1\,{\rm cm}^{-3}$ owing to the deep potential of dark matter cusps. Eventually, dark halos of $\sim 10^4\,M_\odot$ can produce primordial objects. This means that the mass of first-generation objects can be smaller by roughly two orders of magnitude than in previous predictions. Hence, we conclude that the number of Pop III stars formed in an early universe can be significantly larger than in previous predictions.

We have demonstrated that the resolution of dark matter cusps is crucial for thermal instability. Here, we do a convergence test regarding the resolution to verify the present results. We perform an ultra-high resolution simulation (model R512). In Fig. 6, we compare the results between models R256 and R512. We confirm that both give basically the same results. This means that the dark matter cusp resolved down to 1 pc is important for thermal instability. The further inner cusp is not responsible for a significant increase of temperature.

4. Radiation hydrodynamic feedback in first objects

In the previous section, we have shown that two peaks with a separation of ≈60 pc collapse independently. Although each peak could form a fairly massive star of $\gtrsim 40\,M_\odot$, [16] there is a difference in free-fall time of $\sim 5 \times 10^6$ years. Hence, the first peak forms a massive Pop III appreciably ealier than the 2nd peak, and then the first star irradiates the second collapsing peak with strong UV radiation. Thus, whether the 2nd peak successfully forms a star depends upon the strength of radiative feedback from the first star. The physical mechanism of radiation hydrodynamic feedback has been studied by Susa and Umemura [4], Susa et al. [6], and Hasegawa et al. [5]. We show below the basic physics of radiation hydrodynamic feedback and explore the survival of the 2nd peak under the feedback.

4.1. Basic physics

The properties of Pop III stars in the range of $25\,M_\odot \le M_* \le 120\,M_\odot$ are summarized in Table 2, which is taken from Ref. [17]. Since Pop III stars emit strong ionizing and photo-dissociating radiation, the radiation hydrodynamic feedback is regulated by the propagation of an ionizing front and the shielding from photo-dissociating radiation. If a collapsing core is irradiated by an ionizing source located at a distance D, the propagation speed of the ionization front (I-front) in the core is given by

$$v_{\rm IF} = 21\,{\rm km\,s^{-1}} \left(\frac{\dot{N}_{\rm ion}}{10^{50}\,{\rm s^{-1}}}\right) \left(\frac{D}{20\,{\rm pc}}\right)^{-2} \left(\frac{n_{\rm core}}{10^3\,{\rm cm^{-3}}}\right)^{-1}, \tag{4.1}$$

if recombination is neglected, where $\dot{N}_{\rm ion}$ is the number of ionizing photons per unit time and $n_{\rm core}$ is the number density in the cloud core. The sound speed in regions cooled by H_2 is $a_1 \approx 1\,{\rm km\,s^{-1}}$, while that in the ionized regions is $a_2 \approx 10\,{\rm km\,s^{-1}}$. If the density of the cloud core is low or the ionizing radiation flux is strong, then $v_{\rm IF} > 2a_2$ and therefore the I-front becomes R-type. If we focus on a core collapsing in a self-similar fashion [9], the core size $r_{\rm core}$ is on the order of $a_1 t_{\rm ff}$,

where $t_{\rm ff}$ ($\simeq \sqrt{\pi/G\rho_{\rm core}}$) is the free-fall time. Then, the propagation time of the R-type front across the core satisfies $t_{\rm IF} \equiv r_{\rm core}/v_{\rm IF} < (a_1/2a_2)t_{\rm ff} < t_{\rm ff}$. This means that an R-type front sweeps the core before the core collapses in the free-fall time. Thus, the core is likely to undergo photo-evaporation. On the other hand, if the density of the cloud core is high enough or the source distance is large, then $v_{\rm IF} < a_1^2/2a_2$ and a D-type I-front emerges. The propagation time of a D-type front across the core satisfies $t_{\rm IF} > (2a_2/a_1)t_{\rm ff} > t_{\rm ff}$. Thus, the core can collapse before the I-front sweeps the core.

However, the above arguments are based on the assumption that the ionizing photon flux does not change during the propagation of the I-front. The core could be self-shielded from the ionizing radiation if $\dot{N}(\pi r_{\rm core}^2/4\pi D^2) < 4\pi r_{\rm core}^3 n_{\rm core}^2 \alpha_{\rm B}/3$, where $\alpha_{\rm B}$ is the recombination coefficient to all excited levels of hydrogen. The critical density for self-shielding is given by

$$n_{\rm shield} \simeq \left(\frac{3\dot{N}_{\rm ion}}{16\pi D^2 a_1 \alpha_{\rm B}}\sqrt{\frac{Gm_{\rm p}}{\pi}}\right)^{2/3} = 5.1\,{\rm cm}^{-3}\left(\frac{\dot{N}_{\rm ion}}{10^{50}{\rm s}^{-1}}\right)^{2/3}\left(\frac{D}{20\,{\rm pc}}\right)^{-4/3}\left(\frac{a_1}{1\,{\rm km\,s}^{-1}}\right)^{-2/3}. \tag{4.2}$$

If $n_{\rm core} > n_{\rm shield}$, the ionizing photon flux diminishes significantly during the I-front propagation. Hence, even if the I-front is R-type on the surface of the cloud core, the front can change to M-type accompanied by a shock, and eventually to D-type inside the core [33].

In contrast to ionizing radiation, H_2 dissociating radiation in the LW band (11.26–13.6 eV) is less shielded [32]. The self-shielding of the LW band flux ($F_{\rm LW}$) is expressed by

$$F_{\rm LW} = F_{\rm LW,0} f_{\rm sh}(N_{\rm H_2,14}) \tag{4.3}$$

where $F_{\rm LW,0}$ is the incident flux, $N_{\rm H_2,14} = N_{\rm H_2}/10^{14}\,{\rm cm}^{-2}$ is the normalized H_2 column density, and

$$f_{\rm s}(x) = \begin{cases} 1, & x \le 1 \\ x^{-3/4}, & x > 1. \end{cases} \tag{4.4}$$

Hence, if the column density of H_2 molecules ahead of the I-front is high enough, H_2 dissociating radiation can be shielded. Since H_2 molecules form with the catalysis of free electrons, the shielding of dissociating radiation is intimately coupled with the propagation of the I-front.

4.2. START: Accelerated radiation hydrodynamic scheme

In order to perform the radiation hydrodynamic (RHD) simulations more effectively, we have recently developed a novel RHD code called *START* (SPH with Tree based Accelerated Radiation Transfer), which is designed to solve the transfer of UV photons from numerous sources [41]. In *START*, the optical depth between a radiation source and an SPH particle is evaluated with the same method as in the *RSPH* code [35]. In contrast to the corresponding method proposed by Kessel-Deynet and Burkert [42], the evaluation of the optical depth between a radiation source and a target SPH particle is performed only once by using information on its upstream particle. Thus, the cost for each ray-tracing turns out to be proportional to $N_{\rm SPH}$, where $N_{\rm SPH}$ is the number of SPH particles. In addition to the reduction of the cost for each ray-tracing, the effective number of radiation sources for each target SPH particle is diminished by utilizing an oct-tree structure of radiation sources. Like the Barnes–Hut tree method [43] that is frequently used for calculating the gravitational force, if a cell containing some radiation sources is far enough from a target SPH particle, all radiation sources in the cell are regarded as virtual luminous sources. As a result, the computational cost to evaluate optical

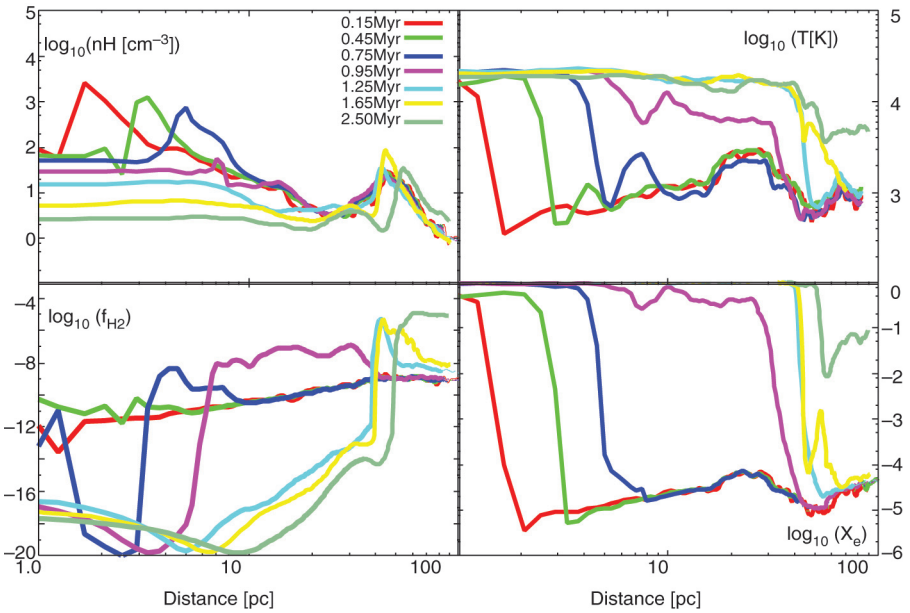

Fig. 7. Time variations of gas density, temperature, H_2 fractions, and ionization degree along the line connecting two peaks are shown at the epochs from 0.15×10^6 to 2.5×10^6 years. The distance is measured from the first peak. The 2nd peak is located at ∼60 pc.

depths from all radiation sources to all SPH particles is proportional to $O(N_{\rm SPH} \log N_s)$. With this code, we can precisely solve the transfer of recombination photons, which is often treated with an on-the-spot approximation. Another important and useful feature of *START* is that the spatial resolution is adaptively enhanced in high density regions, since SPH particles are directly used for the radiative transfer grids. Here, using *START*, we consistently solve the gas and dark matter dynamics coupled with the radiative transfer of UV photons and non-equilibrium chemical reactions for 6 species: e^-, H^+, H, H^-, H_2, and H_2^+.

4.3. Radiation hydrodynamic feedback

We use the results obtained in the previous section, where two dark matter halos host gas clumps, and the separation between the halos is ∼60 pc. The whole simulation box size is 2 kpc (physical) on a side. The particle mass is 0.08 $M_\odot$ for an SPH particle, and 0.38 $M_\odot$ for a DM particle, respectively. We assume a source Pop III star with a mass of 120 $M_\odot$, and place it at the highest density peak. Then, we start the RHD simulations, where not only direct UV photons from the source Pop III star but also diffuse photons produced via recombination processes are considered. After the lifetime of the source star ($t = 2.5 \times 10^6$ years), direct UV photons from the source star are turned off, but the transfer of diffuse photons is continuously solved. After the source star dies, the supernova explosion may make an impact on the collapsing core, which is not treated in this paper and will be explored elsewhere.

The evolution from 0.15×10^6 to 2.5×10^6 years obtained by the radiation hydrodynamic simulation is presented in Fig. 7, where time variations of gas density, temperature, H_2 fractions, and ionization degree along the line connecting two peaks are shown. The distance is measured from the first peak, and the 2nd peak is originally located at ∼ 60 pc. In the early stage before $t = 0.75 \times 10^6$ years, a shock precedes a D-type I-front. Before UV irradiation, the H_2 fraction at the 2nd peak is several 10^{-4}, as shown in Fig. 5. However, as shown in Fig. 7, the H_2 fraction at the 2nd peak is reduced to a level of 10^{-9} due to photo-dissociating radiation, although the H_2 fraction

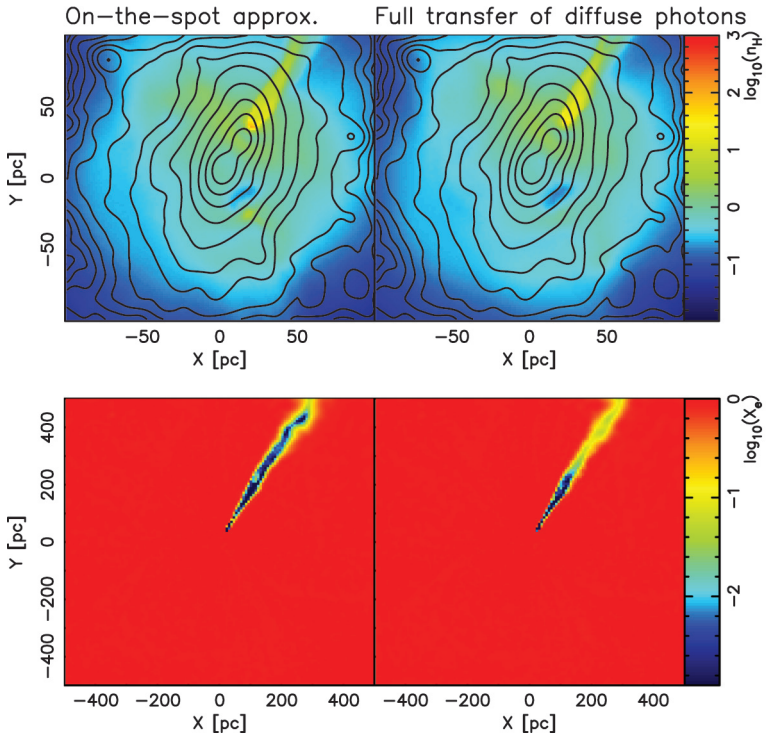

Fig. 8. Snapshots for the gas density (*upper row*), and the ionization degree (*lower row*) at 2.5×10^6 years. The initial distribution at $t = 0.0 \times 10^6$ years corresponds to the rightmost panel of Fig. 4. The origin, $(x, y) = (0, 0)$ [pc], is set to be the position where the highest peak was originally located, and the 2nd peak was originally located at $(x, y) = (20, 50)$ [pc]. The contours show the dark matter distributions. The left panels are the results under the on-the-spot approximation, while the right panels show the results of full radiation-hydrodynamic simulations solving the transfer of diffuse photons.

near the I-front is slightly enhanced. After this stage, the I-front changes into R-type. The evolution until this early stage is very similar to the corresponding results shown by Kitayama et al. [7] or Yoshida et al. [8]. However, unlike these previous studies, the I-front changes into D-type again at $t \sim 1.25 \times 10^6$ years due to the presence of the 2nd peak. Then, an H_2 shell with an H_2 fraction of $\sim 10^{-4}$ forms ahead of the 2nd peak thanks to the catalysis of free electrons. This H_2 shell shields photo-dissociating radiation significantly, and consequently the H_2 fraction at the 2nd peak is restored to $\sim 10^{-4}$. Simultaneously, the envelope of the 2nd peak is stripped by the shock associated with the I-front.

The ionization around the 2nd peak is dependent on the treatment of UV radiation transfer. In Fig. 8, the results under the on-the-spot approximation are compared to those of full RHD simulations solving the transfer of diffuse photons at the epoch of 2.5 Myr. As shown in the top panels of Fig. 8, the diffuse UV radiation hardly affects the gas distribution in the 2nd peak, because the mean free path of ionizing photons is quite short there. Thus, the impact of the diffuse UV radiation on the 2nd peak is diminutive. On the other hand, the difference of the ionized fractions in the outer envelope is obvious behind the 2nd peak. The full RHD simulations show that diffuse UV radiation can ionize the gas behind the 2nd peak, since the photon mean free path is relatively long in this region. Therefore, solving the transfer of diffuse UV radiation is of great significance in computing the ionization of low-density gas, e.g., intergalactic medium.

The later evolution of the 2nd peak is determined by the interplay of the shielding from photo-dissociating radiation and the stripping by an ionization-front shock. In Fig. 9, the later

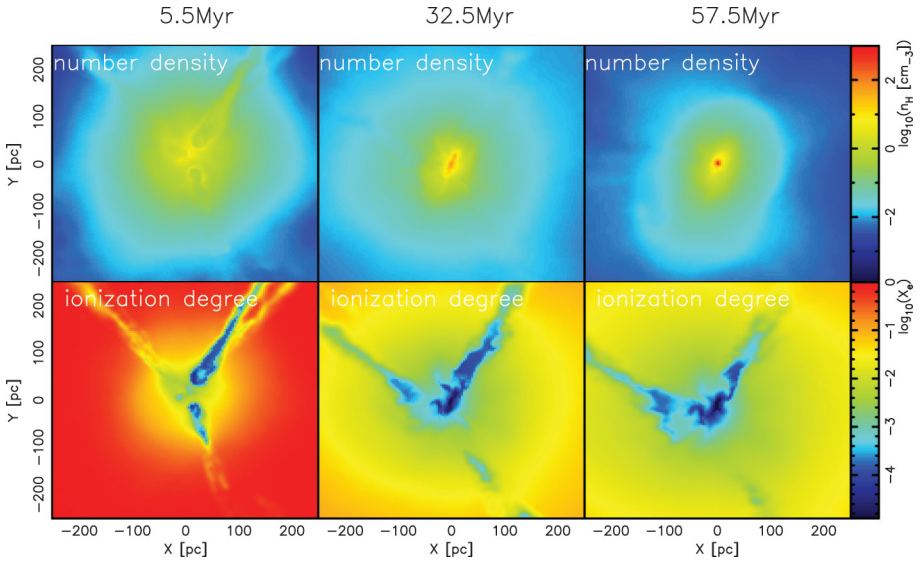

Fig. 9. The late-phase evolution of the 2nd peak is shown at 5.5×10^6, 32.5×10^6, and 57.5×10^6 years. The origin, $(x, y) = (0, 0)$ [pc], is set to be the position where the highest peak was originally located, and the 2nd peak was originally located at $(x, y) = (20, 50)$ [pc]. The gas density is shown in the upper row, and the ionization degree is shown in the lower row.

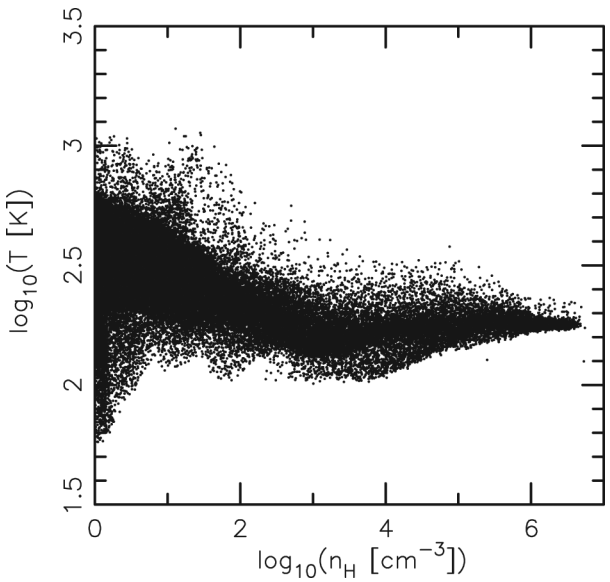

Fig. 10. Temperature versus density at the end of the simulation.

evolution in full RHD simulations is presented at 5.5×10^6, 32.5×10^6, and 57.5×10^6 years, where the distributions of density and ionization degree are shown. After $t = 2.5 \times 10^6$ years, no UV radiation is emitted from the source. Thus, recombination gradually increases the neutral fractions. But, diffuse UV radiation from the recombination ionizes the shadowed region behind the 2nd peak. Although the central density of the 2nd peak decreases via the photo-ionization and a shock associated with the ionization front, the 2nd peak eventually collapses. In Fig. 10, the density of the 2nd peak is shown against temperature. This figure shows that the 2nd peak continues to collapse after thermal instability, irrespective of the radiative feedback.

4.4. Analytic criteria

Here, we derive analytic criteria for the feedback, based on the argument by Hasegawa et al. [5]. Susa [34] explored the photo-dissociation feedback of a Pop III star with 120 $M_\odot$ on a neighboring prestellar core by RHD simulations without ionizing radiation. Susa found that a condition for the collapse of a neighboring core is approximately determined by $t_{\rm dis} = t_{\rm ff}$, where $t_{\rm dis}$ is the photo-dissociation timescale in the core and $t_{\rm ff}$ is the free-fall timescale. Using this condition, the critical distance $D_{\rm cr,d}$, above which a neighboring core is able to collapse, is given by

$$D_{\rm cr,d} = 147\,{\rm pc}\left(\frac{L_{\rm LW}}{5\times10^{23}\,{\rm erg\,s^{-1}}}\right)^{1/2}\left(\frac{n_{\rm c}}{10^3\,{\rm cm^{-3}}}\right)^{-7/16} \times\left(\frac{T_{\rm c}}{300\,{\rm K}}\right)^{-3/4}, \tag{4.5}$$

where $L_{\rm LW}$, $n_{\rm c}$, and $T_{\rm c}$ are the LW luminosity of the source star, the number density of the core, and the temperature of the core, respectively. This equation involves the self-shielding effect by the core. The dependence on the core temperature basically originates in the core radius ($\propto T_{\rm c}^{1/2}$) and an H_2 formation rate in the core ($\propto T_{\rm c}$). Hence, the self-shielding effect is weaker for a lower core temperature. The boundary between the collapse irrespective of ionizing radiation and that with the aid of ionizing radiation can be determined by $D_{\rm cr,d}$. In addition, $D_{\rm cr,d}$ gives a good estimate for less massive source star cases, because the ionizing radiation is relatively weak for less massive stars.

If ionizing radiation is included, we should also incorporate the shielding effect by an H_2 shell, which is formed with the catalysis of free electrons. Here, we derive a new criterion including this effect. Since a cloud collapses in a self-similar fashion before UV irradiation, the density profile of the outer envelope in the cloud is well expressed as

$$n(r) = n_{\rm c}\left(\frac{r_{\rm c}}{r}\right)^2, \tag{4.6}$$

where $r_{\rm c}$ is the core radius that roughly corresponds to the Jeans scale,

$$r_{\rm c} = \frac{1}{2}\sqrt{\frac{\pi k_B T_{\rm c}}{G m_p^2 n_{\rm c}}}, \tag{4.7}$$

where $m_{\rm p}$ denotes the proton mass. Assuming that the thickness of the H_2 shell is determined by the amount of ionized gas in the envelope and the H_2 fraction in the shell is constant, the H_2 column density of the shell $N_{\rm H_2,sh}$ is given by

$$N_{\rm H_2,sh} = \int_D^{D_{\rm sh}} y_{\rm H_2,sh} n(r) dr = y_{\rm H_2,sh} n_{\rm c} r_{\rm c}^2 \frac{D - D_{\rm sh}}{D D_{\rm sh}}, \tag{4.8}$$

where $D_{\rm sh}$ and $y_{\rm H_2,sh}$ are the distance between the cloud core and the H_2 shell, and the H_2 fraction in the shell, respectively. Here, $D_{\rm sh}$ is set to be the position where the number of recombination per unit time in the ionized region around a source star balances the number rate of incident ionizing photons, since the H_2 shell appears ahead of the ionization front. Hence, $D_{\rm sh}$ satisfies

$$\frac{\dot{N}_{\rm ion}\pi D_{\rm sh}^2}{4\pi(D - D_{\rm sh})^2} = 2\pi\alpha_{\rm B}\int_D^{D_{\rm sh}} n(r)^2 r^2 dr = 2\pi\alpha_{\rm B} n_c^2 r_c^4 \frac{D - D_{\rm sh}}{D D_{\rm sh}}. \tag{4.9}$$

Using Eqs. (4.8) and (4.9), we obtain

$$N_{\mathrm{H_2,sh}} = y_{\mathrm{H_2,sh}} n_{\mathrm{c}}^{1/3} r_{\mathrm{c}}^{2/3} D^{-2/3} \left(\frac{\dot{N}_{\mathrm{ion}}}{8\pi \alpha_{\mathrm{B}}} \right)^{1/3}. \tag{4.10}$$

Because of the intense LW radiation, the H_2 abundance at the shell is in chemical equilibrium. Therefore, $y_{\mathrm{H_2,sh}}$ is given by

$$y_{H_2,sh} = \frac{n(D_{\mathrm{sh}}) y_{\mathrm{e,sh}} k_{\mathrm{H^-}}}{k_{\mathrm{dis}}}, \tag{4.11}$$

where $y_{\mathrm{e,sh}}$ is the electron fraction at the H_2 shell and $k_{\mathrm{H^-}}$ is the reaction rate of the H^- process by (3.1). In this case, we should consider the self-shielding effect by the shell itself. As a result, these rates are

$$k_{\mathrm{H^-}} = 1.0 \times 10^{-18} T_{\mathrm{sh}}\, \mathrm{cm^{-3}\, s^{-1}}, \tag{4.12}$$

$$k_{\mathrm{dis}} = 1.13 \times 10^8 F_{\mathrm{LW,sh}} f_{\mathrm{s}} \left(\frac{N_{\mathrm{H_2,sh}}/2}{10^{14}\, \mathrm{cm^{-2}}} \right) \mathrm{s^{-1}}, \tag{4.13}$$

where T_{sh} and $F_{\mathrm{LW,sh}}$ are the temperature at the shell, and the LW flux from the star in the absence of the shielding effect, $F_{\mathrm{LW,sh}} = L_{\mathrm{LW}}/4\pi(D - D_{\mathrm{sh}})^2$. f_{s} is the self-shielding function, which is given by (4.4). Combining Eqs. (4.10)–(4.13) with the assumption of $y_{\mathrm{e,sh}} = 0.05$ and $T_{\mathrm{sh}} = 2000\,\mathrm{K}$ as shown in the present numerical results, we have

$$y_{\mathrm{H_2,sh}} = 1.0 \times 10^{-6} \left(\frac{\dot{N}_{\mathrm{ion}}}{10^{50}\, \mathrm{s^{-1}}} \right)^{11/3} \left(\frac{L_{\mathrm{LW}}}{5 \times 10^{23} \mathrm{erg\ s^{-1}}} \right)^{-4} \times \left(\frac{T_{\mathrm{c}}}{300\,\mathrm{K}} \right)^{-1/3} \left(\frac{D}{40\,\mathrm{pc}} \right)^{2/3}, \tag{4.14}$$

$$N_{\mathrm{H_2,sh}} = 5.8 \times 10^{14} \left(\frac{\dot{N}_{\mathrm{ion}}}{10^{50}\, \mathrm{s^{-1}}} \right)^{4} \times \left(\frac{L_{\mathrm{LW}}}{5 \times 10^{23}\, \mathrm{erg\, s^{-1}}} \right)^{-4} \mathrm{cm^{-2}}. \tag{4.15}$$

It should be noted that $N_{\mathrm{H_2,sh}}$ is independent of the core temperature T_{c}, but is determined solely by the ratio of $\dot{N}_{\mathrm{ion}}$ to L_{LW} with strong dependence.

Multiplying L_{LW} in Eq. (4.5) by

$$f_{\mathrm{s,sh}} \equiv f_{\mathrm{s}} \left(\frac{N_{\mathrm{H_2,sh}}}{10^{14}\, \mathrm{cm^{-2}}} \right), \tag{4.16}$$

we obtain the critical distance as

$$D_{\mathrm{cr,sh}} = 147\,\mathrm{pc} \left(\frac{L_{\mathrm{LW}} f_{\mathrm{s,sh}}}{5 \times 10^{23}\, \mathrm{erg\, s^{-1}}} \right)^{1/2} \left(\frac{n_{\mathrm{c}}}{10^3\, \mathrm{cm^{-3}}} \right)^{-7/16} \times \left(\frac{T_{\mathrm{c}}}{300\,\mathrm{K}} \right)^{-3/4}, \tag{4.17}$$

in which both shielding effects by the core and the H_2 shell are taken into account. In particular, if $N_{H_2,sh}$ is larger than $10^{14}\,cm^{-2}$, the critical distance can be expressed as

$$D_{cr,sh} = 78.8\,pc \left(\frac{L_{LW}}{5\times10^{23}\,erg\,s^{-1}}\right)^{2} \left(\frac{\dot{N}_{ion}}{10^{50}\,s^{-1}}\right)^{-3/2} \times \left(\frac{n_c}{10^3\,cm^{-3}}\right)^{-7/16} \left(\frac{T_c}{300\,K}\right)^{-3/4}. \quad (4.18)$$

Based upon Eq. (4.15), the shielding effect by the shell becomes weaker as $\dot{N}_{ion}/L_{LW}$ decreases. Equation (4.18) gives a criterion of distance, above which a cloud core can collapse through the shielding of photo-dissociation radiation by an H_2 shell. The present results of radiation hydrodynamic simulations show that a cloud located at 60 pc collapses under the UV feedback. This is broadly consistent with this analytic criterion. In the present simulations, the peak separation was ∼60 pc. Whether this separation is a typical value has not been revealed in the present analysis. A case study using more realizations of random fluctuations is needed, and this is left for future work.

5. Fragmentation of a first protostellar disk and radiative feedback

As stated in the introduction, theoretical efforts in the last decade have revealed that the very first stars are more massive than stars forming in present-day galaxies. A few years before, it was believed that they are very massive ($>100\,M_\odot$). However, recent numerical studies using the sink particle technique suggest that, owing to the fragmentation in an accretion phase, they could be $O(10)\times M_\odot$ or less, and eventually they form a multiple stellar system [18–20]. In some cases, it might also be possible for sub-solar mass first stars to form from such fragments. In addition, recent 2D radiation hydrodynamic simulations revealed that UV radiative feedback from first protostars is quite important to quench the mass accretion onto the first protostar [16].

In this framework, we incorporate UV radiative feedback effects into 3D chemo-hydrodynamical simulations, in order to follow the fragmentation of an accreting gas disk in realistic circumstances.

5.1. Numerical method with sink particles

We perform numerical experiments using the *RSPH* code developed by ourselves [35]. We set the initial condition of a cloud to be a Bonner–Evert sphere with a density of $10^4\,cm^{-3}$ and a temperature of 200 K, at the "loitering" phase of a collapsing primordial prestellar cloud. We add rigid rotation with an angular velocity of $\Omega = 2\times10^{-14}\,s^{-1}$, which is comparable to rotation in cosmological simulations [3].

In order to follow the accretion phase, we introduce the sink particle technique in the *RSPH* code. In the case where the density at the position of an SPH particle exceeds $10^{13}\,cm^{-3}$, it is regarded as a sink particle. Also, particles that enter a sphere of radius 20 AU centered on each sink particle are absorbed in the sink particle if they are gravitationally bounded. In the present simulations, the mass of the SPH particle is $6\times10^{-4}\,M_\odot$. Following previous studies [36], the corresponding mass resolution is $\sim0.1\,M_\odot$, which is well below the Jeans mass of the disk at 1000 K, and that allows us to investigate the gravitational fragmentation of the disk. In the present work, we focus on the effects of Lyman–Werner radiation from the first protostar on the fragmentation of the disk, and the resultant accretion rate onto the first protostars. We solve non-equilibrium processes for H_2 formation. The transfer of the Lyman–Werner radiation is solved utilizing the self-shielding function [37]. The luminosity and the effective temperature of the protostars are assessed by regarding the masses and the mass

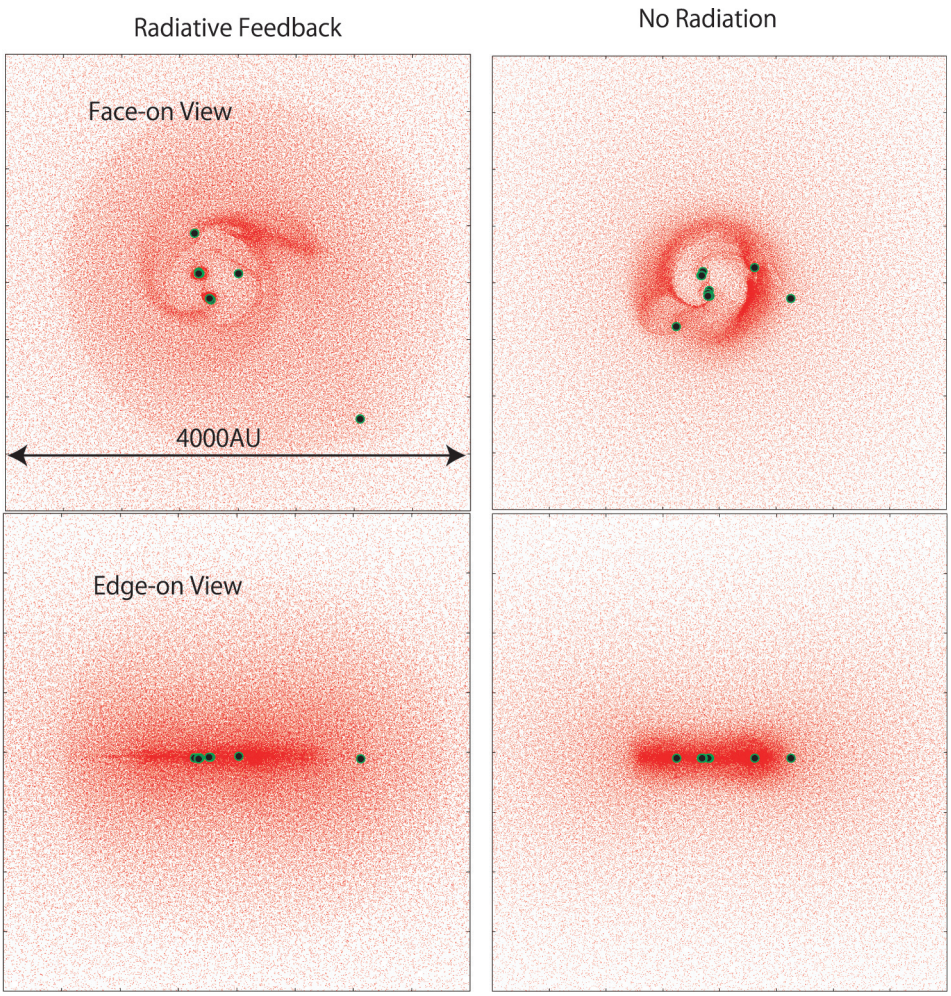

Fig. 11. Snapshots at 5500 years after the first sink formation are shown. Red dots represent SPH particles, while black dots are sink particles. Left panels (face-on/edge-on view) are the results with radiative feedback, while the right panels are those without radiative feedback.

accretion rates of the sink particles as those of the protostars. In paticular, we interpolate the tables of luminosity and temperature generated by Hosokawa et al. [38]. Although the effects of photo-ionization are also important, we could not treat them due to the lack of spatial resolution. We leave them for future work.

5.2. Radiative feedback in a first protostellar disk

Figure 11 shows the numerical results, where the snapshots of distributions are presented at 5500 years. Left panels show the edge-on/face-on views of the gas disk in the inner $(4000\,\mathrm{AU})^3$ box of the simulated region with radiative feedback, whereas the right panels show those for the case without radiative feedback. In both cases, we observe that several sink particles are formed (black circles), while the gas particle distributions (red dots) are more extended in the case with radiative feedback. This difference is a consequence of the H_2 photo-dissociation process. The two panels in Fig. 12 show bird's-eye views of the gas disk around the protostars at two epochs 1600 and 5500 years. At the later epoch (right panel), the polar region of the gas disk is highly dissociated by the radiation from the sink particles. The dissociated region is heated up to $7000 - 8000\,\mathrm{K}$, due to accretion

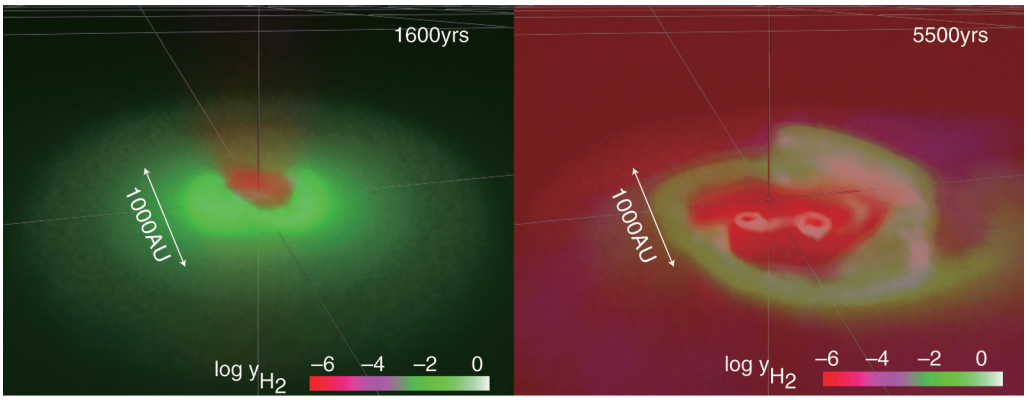

Fig. 12. Bird's-eye view of the gas disk around the first sink at two epochs. Transparency describes the gas density, while color shows the logarithmic fraction of H_2 molecules (y_{H_2}). At an earlier epoch (1600 years), the conical zone at the center is highly dissociated (red gas), while the other region is still unaffected by the central source. On the other hand, at a later epoch (5500 years), only dense cold streams (white/green gas) orbiting around the center sustain a significant amount of H_2, while the other less dense region is totally dissociated.

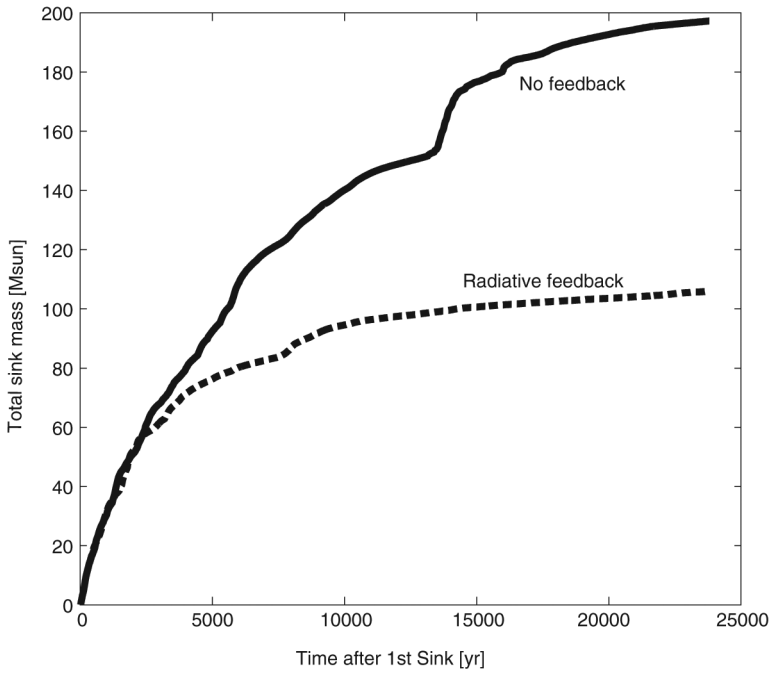

Fig. 13. Time evolution of total sink mass. The two curves correspond to the cases with/without radiative feedback.

shocks and chemical heating. In the absence of photo-dissociating radiation, H_2 dissociation cooling should almost cancel H_2 formation heating. But, in the photo-dissociated region, H_2 formation heating is of great significance, since H_2 dissociation cooling is negligible in such environments.

The "heated bubble" originating from the absence of coolant as well as chemical heating by photo-dissociation reduces the mass accretion rate onto the sink particles. In fact, the total accreted mass after 24 000 years is ∼50% smaller than the mass without radiative feedback (Fig. 13). Thus, photo-dissociation is an important effect in controlling the final mass of the first stars. On the other hand, it is worth noting that photo-dissociation feedback cannot quench the fragmentation of the gas disks.

We observe fragmentation of the disk in both cases with and without radiative feedback, and the numbers of sink particles are ∼10.

We also find that a few sinks are kicked away from the central part of the host gas cloud via the gravitational three-body interaction. As a result, the mass accretion onto these sinks is basically shut off. We find that some of these sinks do not grow to more than 0.8 $M_\odot$. The main sequence lifetime of such low mass stars is $\sim 2 \times 10^{10}$ years. If we regard these sink particles as "stars", we might be able to find the "real first stars" in the Galactic halo.

6. Evolution of first galaxies by internal UV feedback

UV radiation affects the chemo-thermal and dynamical evolution of galaxies through photo-ionization, -heating, and -dissociation processes. Although the importance of such UV feedback on structure formation in the universe was pointed out in the 1980s, no calculation of 3D hydrodynamics coupled with radiative transfer was ever realized until the 2000s. In the last decade, it became possible to perform 3D radiation hydrodynamics (3D-RHD) simulations, thanks to developments in computers and calculation algorithms [39]. The *START* scheme enables us to solve 3D-RHD for numerous radiation sources [41]. In this section, we present the results of RHD simulations on the ionization of first galaxies and the escape of ionizing photons, and thereby demonstrate the necessity of RHD simulations. Here, a ΛCDM cosmology with $(\Omega_\Lambda, \Omega_{\rm m}, \Omega_{\rm b}, h) = (0.73, 0.27, 0.049, 0.71)$ is employed.

6.1. Determination of radiative reaction rates

Once optical depths are determined, radiative reaction rates such as photo-ionization and photo-heating rates can be evaluated. For instance, the ionization rate for the ith chemical species (i.e., H I, He I, or He II) at a position $\mathbf{r}$ is generally given by

$$k_{ion,i}(\mathbf{r}) = n_i(\mathbf{r}) \int_{\nu_{L,i}}^{\infty} \int \sigma_{\nu,i} \frac{I_{\nu,0} e^{-\tau_\nu(\mathbf{r})}}{h\nu} d\nu \, d\Omega, \tag{6.1}$$

where n_i, $\nu_{L,i}$, and $\sigma_{\nu,i}$ are the number density, the Lyman limit frequency, and the cross-section for the ith species. $I_{\nu,0}$ is the intensity of incident radiation at frequency ν, and τ_ν is the optical depth. Here, we should treat this equation carefully, because it becomes numerically zero where $\tau_\nu(\mathbf{r})$ is much larger than unity. This implies that the ionization rates become zero even if the number of ionizing photons is enough to ionize the medium. This leads to the unphysical feature that the ionization front does not propagate into an optically thick media. To avoid this problem, the form given by

$$k_{ion,i}(\mathbf{r}) = -\frac{1}{4\pi r^2} \frac{d}{dr} \int_{\nu_{L,i}}^{\infty} \frac{n_i(\mathbf{r}) \sigma_{\nu,i}}{(n\sigma)_{tot}} \frac{L_\nu e^{-\tau_\nu(\mathbf{r})}}{h\nu} d\nu, \tag{6.2}$$

is often used instead of Eq. (6.1) so as to conserve the photon number. The photo-heating rates can be similarly evaluated by multiplying the term in the integral by $(h\nu - h\nu_{L,i})$.

6.2. Chemo-thermal evolution coupled with RHD

We update the information on the radiation field at every period of $t_{RT} = 0.1 \times \min(t_{\rm rec}, t_{\rm hydro})$ by solving radiative transfer (RT), where $t_{\rm rec}$ and $t_{\rm hydro}$ are respectively the timescales for the recombination $t_{\rm rec} = 1/n\alpha(T)$ and hydrodynamics $t_{\rm hydro} = h/(|\mathbf{v}| + c_s(T))$, where n, T, h, $\mathbf{v}$, and $c_s(T)$ are the number density, temperature, smoothing length, velocity, and sound velocity of an SPH particle,

respectively. In the case of $t_{\rm hydro} > t_{\rm rec}$, we repeatedly solve the RT at an interval of $t_{\rm rec}$ during $t_{\rm hydro}$. In order to determine $t_{\rm rec}$, we always use only particles on which the relative change of the ionized fraction during previous t_{RT} is greater than 10%. This treatment allows us to effectively reduce the computational cost due to the following two reasons. First, it is often true that high density regions are well self-shielded, thus $t_{\rm rec}$ should be determined among SPH particles that reside outside of the self-shielded regions, otherwise we have to solve RT many times to no avail. Secondly, at a later phase of expansion of an H II region, which is called a D-type ionization front, the ionization equilibrium is almost fulfilled in the H II region, and the change of radiation field is caused mainly by hydrodynamic motion driven by thermal pressure.

When UV feedback is included, the chemical ($t_{\rm chem,i} = n_i/\dot{n}_i$) and thermal ($t_{\rm thermal} = T/\dot{T}$) timescales are generally shorter than t_{RT}. In addition, the set of equations that determine the abundance of chemical species are stiff. Therefore, we implicitly solve the chemo-thermal evolution with subcycle timestep $t_{sub} = \min(t_{\rm chem}, t_{\rm thermal})$. Here note that the ionization rates also vary during t_{RT}, since they are multiplied by $n_i = f_i n/(\mu m_{\rm H})$, where f_i and μ are the fraction of the ith species and the mean molecular weight, respectively.

6.3. Feedback and escape of ionizing radiation in first galaxies

It is important in revealing the cosmic reionization history to clarify how many ionizing photons can escape from galaxies. Previous numerical simulations that evaluate the escape fractions of ionizing photons from galaxies can be categorized into two types: One type is RDH simulations in which UV feedback is consistently taken into account [44,45], and the other is non-RHD simulations in which the transfer of ionizing photons is solved without the back-reactions on chemodynamics caused by UV feedback [46,47]. UV feedback is expected to play a crucial role in the determination of the escape fraction, since the gas in a less massive galaxy is easily evacuated by UV feedback [45]. Thus it is generally expected that the escape fraction from a less massive galaxy is enhanced by UV feedback, although nobody has quantitatively clarified how much the UV feedback impacts the escape fraction. On the other hand, the escape fraction from a massive galaxy is often expected to be insensitive to the UV feedback, since the galaxy hardly loses its gaseous components. However, if the internal density structure of the galaxy is significantly changed by UV feedback, the escape fraction is possibly changed [48].

Here, we investigate the impact of UV feedback on the escape fraction of ionizing photons from a massive halo. We have performed a cosmological RHD simulation [40], where the radiative transfer of UV radiation from individual stellar particles is solved together with the hydrodynamics. In order to evaluate an ionizing photon production rate that depends on stellar age, we have calculated population synthesis with PÉGASE [49] in advance of the simulation, and used the obtained rate in the simulation. The masses of the SPH and dark matter particles are respectively $4.8 \times 10^4\ M_\odot$ and $2.9 \times 10^5\ M_\odot$. Thus, we can resolve low mass halos down to $M_{\rm halo} \approx 3 \times 10^7\ M_\odot$ with 100 particles. For the reference case, we have also performed a pure hydrodynamic (non-RHD) simulation for the same initial conditions and cosmological parameters, where the UV radiation transfer is not coupled and therefore no effect by UV feedback is included. In a non-RHD simulation, the escape fraction of ionizing photons is assessed by solving the UV radiative transfer as a post process using the density distributions obtained by a pure hydrodynamic simulation.

We choose the most massive halo at $z = 6.0$ in each of the simulations. Hereafter, we call the halo in the RHD simulation Halo-R, and that in the non-RHD simulation Halo-H. The properties of these halos are summarized in Table 3. Here, we should mention that the halos are

Table 3. Properties of simulated halos.

Name	$M_{\rm halo}[M_\odot]$	$M_b[M_\odot]$	$M_*[M_\odot]$	$\dot{N}_{int}[1/{\rm s}]$	$f^{\rm a)}_{\rm e,HI}$	$f^{\rm b)}_{\rm e,HeI}$	$f^{\rm c)}_{\rm e,HeII}$
Halo-R (w/ UV)	6.8×10^9	1.2×10^9	2.9×10^7	5.9×10^{52}	0.31	0.35	0.13
Halo-H (w/o UV)	6.7×10^9	1.0×10^9	1.0×10^8	3.6×10^{53}	0.15	0.14	0.11

a) Escape fraction of photons ionizing H I.
b) Escape fraction of photons ionizing He I.
c) Escape fraction of photons ionizing He II.

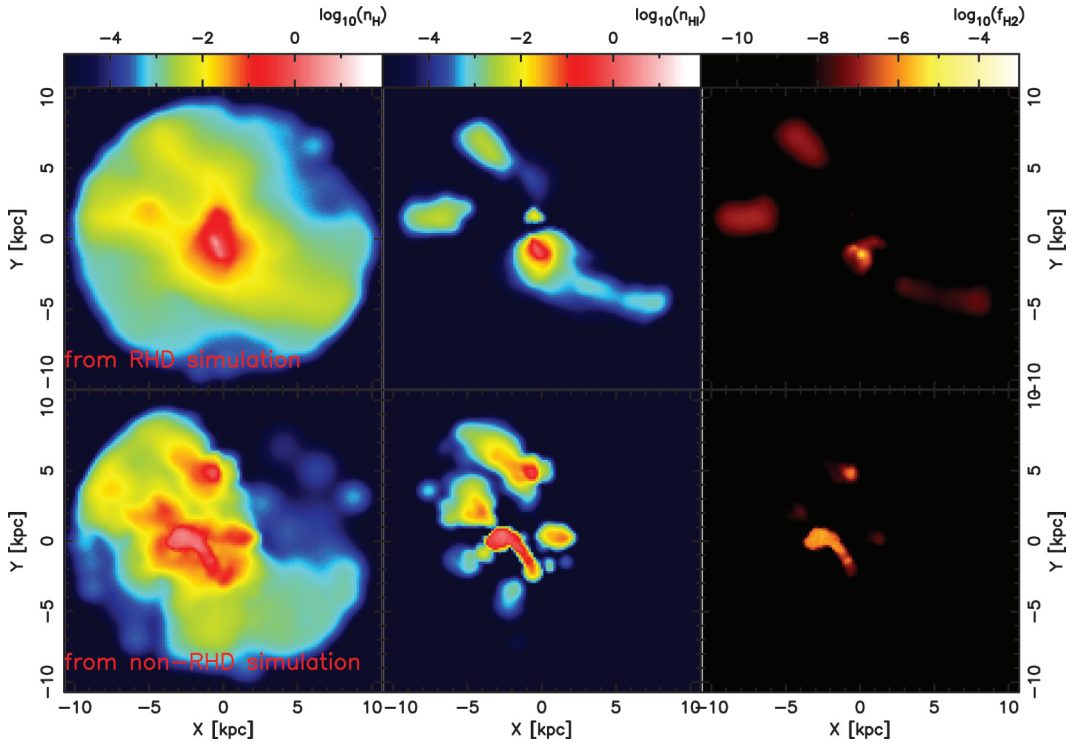

Fig. 14. Maps of hydrogen number densities, H I number densities, and H_2 fractions are shown from left to right. The slice thickness is 2 kpc. The upper panels show the halo taken from the RHD cosmological simulation (Halo-R), while the bottom panels show the halo taken from the non-RHD cosmological simulation (Halo-H) with the post-processing RT calculation done by the procedure described in the text.

sufficiently massive and hardly lose their baryonic components via photo-evaporation. Actually, the resultant ratio of the baryon mass to the halo mass is $M_b/M_{\rm halo}\approx 0.16$, which is comparable to $\Omega_b/\Omega_{\rm m}=0.18$.

Figure 14 shows the numerical results, where number densities, ionized fractions, and H_2 fractions are shown. For Halo-R, the ionized structures are calculated in the RHD simulation, and the escape fractions of H I, He I, and He II ionizing photons are obtained. On the other hand, in order to assess the escape fractions of ionizing photons for Halo-H, we solve the radiative transfer as post-processing until the ionization equilibrium is reached at all positions. Hereafter, we call this procedure the post-proccesing RT. This is a method frequently used to estimate the escape fraction [46,47]. We count the number of escaping photons at $2\times64\times64$ virtual grid points placed outside the halo. The upper panels in Fig. 14 show the RHD simulation, while lower panels are the non-RHD simulations with the post-processing RT calculation.

As seen in Fig. 14, a high density peak forms near the center in Halo-R, where the gas is self-shielded from ionizing radiation and H_2 molecules form efficiently. This central peak allows further star formation. The gas in the remaining regions is quite smoothly distributed and mostly ionized. This is thought to be the consequence of radiation hydrodynamic feedback by photo-ionization of H, photo-dissociation of H_2, and photo-heating. On the other hand, several density peaks appear in Halo-H, where the gas in each peak is self-shielded from ionizing radiation. Recently, Fernandez and Shull have pointed out that the escape fraction sensitively depends on the internal structure in a galaxy [48]. The clumpy structure in the present simulation can reduce the escape fraction of ionizing photons from the galaxy. The resultant escape fractions averaged over all directions are presented in Table 3. The escape fractions from Halo-R are actually higher than those from Halo-H by a factor of 2. It has often been argued that UV feedback would increase the escape fractions for a less massive halo because of the mass loss by UV heating [45]. Interestingly, the present results show that the escape fractions can be enhanced by UV feedback even in a massive halo. As for reionization, what is important is the product of the intrinsic ionizing photon production rate $\dot{N}_{\rm int}$ multiplied by the escape fraction $f_{\rm e}$. The product is three times higher in Halo-H, since the star formation rate is significantly higher in Halo-H.

The dependence of UV feedback on the galaxy mass is unclear in the present analysis, and hence a statistical study is needed. But, naively, the impacts of UV feedback on the escape fractions and star formation are expected to be more dramatic for less massive halos. Therefore, the present results demonstrate that RHD simulations are requisite to reveal the sources of the cosmic reionization.

7. Summary

In this paper, we have explored the formation of first objects and first galaxies with radiative feedbacks. The mass of first objects has been investigated by high-resolution hydrodynamic simulations. As a result, it has been revealed that the dark matter cusp potential, if it is resolved well, allows a smaller mass object to collapse, and then the first object mass could be reduced by roughly two orders of magnitude compared to previous predictions. This implies that the number of Pop III stars formed in the early universe could be significantly larger than hitherto thought. Furthermore, radiation hydrodynamic simulations with feedback by photo-ionization and photo-dissociation photons have shown that multiple stars can form in a $10^5\,M_\odot$ halo. Also, the analytic criteria for radiation hydrodynamic feedback are presented.

In addition, the fragmentation of an accreting disk around a first protostar has been studied with photo-dissociation feedback. As a result, it is found that the fragmentation is not quenched by photo-dissociation feedback, but the "heated bubble" resulting from the photo-dissociation can reduce the mass accretion rate onto protostars. Also, protostars as small as $0.8\,M_\odot$ can be ejected through gravitational three-body interaction and evolve while keeping their mass. Such small stars might be detected as the "real first stars" in the Galactic halo.

Finally, radiation hydrodynamic simulations have been performed to assess the impact of UV feedback on first galaxies. By comparing radiation hydrodynamic simulations to pure hydrodynamic simulations, we have found that UV feedback enhances the escape fraction by a factor of 2 even in a massive halo. However, the product of the intrinsic ionizing photon production rate multiplied by the escape fraction is three times higher in the case without UV feedback than in the case with UV feedback. These results imply that UV feedback deserves careful consideration to reveal the cosmic reionization history.

Acknowledgments

Numerical simulations were performed with the *FIRST* simulator and *T2K-Tsukuba* at the Center for Computational Sciences in the University of Tsukuba, and also Blue Gene/P Babel at the SNRS computing center: IDRIS. This work was supported in part by the *FIRST* project based on a Grant-in-Aid for Specially Promoted Research in MEXT (16002003) and a JSPS Grant-in-Aid for Scientific Research (S) (20224002), by a JSPS Grant-in-Aid for Young Scientists B: 24740114, by MEXT HPCI STRATEGIC PROGRAM, and by the French funding agency ANR (ANR-09-BLAN-0030).

References

[1] M. Tegmark et al., Astrophys. J. **474**, 1 (1997).
[2] T.M. Fuller and H.M.P. Couchman, Astrophys. J. **544**, 6 (2000).
[3] N. Yoshida, T. Abel, L. Hernquist, and N. Sugiyama, Astrophys. J. **592**, 645 (2003).
[4] H. Susa, H., and M. Umemura, Astrophys. J. Lett. **645**, L93 (2006).
[5] K. Hasegawa, M. Umemura, and H. Susa, Mon. Not. R. Astron. Soc. **395**, 1280 (2009).
[6] H. Susa, M. Umemura, and K. Hasegawa, Astrophys. J. **702**, 480 (2009).
[7] T. Kitayama, N. Yoshida, H. Susa, and M. Umemura, Astrophys. J. **613**, 631 (2004).
[8] N. Yoshida, S. P. Oh, T. Kitayama, and L. Hernquist, Astrophys. J. **663**, 687 (2007).
[9] K. Omukai and R. Nishi, Astrophys. J. **508**, 141 (1998).
[10] V. Bromm, P. S. Coppi, and R. B. Larson, Astrophys. J. **527**, L5 (1999).
[11] T. Abel, G. L. Bryan, and M. L. Norman, Astrophys. J. **540**, 39 (2000).
[12] T. Abel, G. L. Bryan, and M. L. Norman, Science **295**, 93 (2002).
[13] N. Yoshida, K. Omukai, and L. Hernquist, Science **321**, 669 (2008).
[14] F. Nakamura and M. Umemura, Astrophys. J. **548**, 19 (2001).
[15] B. W. O'Shea and M. L. Norman, Astrophys. J. **654**, 66 (2007).
[16] T. Hosokawa, K. Omukai, N. Yoshida, and H. W. Yorke, Science **334**, 1250 (2011).
[17] D. Schaerer, Astron. Astrophys. **382**, 28 (2002).
[18] P. C. Clark, S. C. O. Glover, R. J. Smith, T. H. Greif, R. S. Klessen, and V. Bromm, Science **331**, 1040 (2011).
[19] A. Stacy, T. H. Greif, and V. Bromm, Mon. Not. R. Astron. Soc. **403**, 45 (2010).
[20] T. H. Greif et al., Astrophys. J. **737**, 75 (2011).
[21] T. Fukushige, J. Makino, and A. Kawai, Publ. Astron. Soc. Jpn. **57**, 1009 (2005).
[22] M. Umemura, H. Susa, T. Suwa, and D. Sato, AIP Conf. Proc. **990**, 386 (2008).
[23] M. Umemura et al., Proc. IAU Symp. 255 (on-line version) (Cambridge University Press, Cambridge, UK, 2008).
[24] M. Umemura, H. Susa, and T. Suwa, AIP Conf. Proc. **1238**, 101 (2010).
[25] J. F. Navarro, C.S. Frenk, and S.D.M. White, Astrophys. J. **490**, 493 (1997).
[26] T. Fukushige and J. Makino, Astrophys. J. **477**, L9 (1997).
[27] B. Moore, S. Ghigna, F. Governato, G. Lake, T. Quinn, J. Stadel, and P. Tozzi, Astrophys. J. **524**, L19 (1999).
[28] Y. P. Jing and Y. Suto, Astrophys. J. **529**, 69 (2000).
[29] T. Fukushige, A. Kawai, and J. Makino, Astrophys. J. **606**, 625 (2004).
[30] J. Diemand et al., Nature **454**, 735 (2008).
[31] V. Springel et al., Mon. Not. R. Astron. Soc. **391**, 1685 (2008).
[32] B. T. Draine and F. Bertoldi, Astrophys. J. **468**, 269 (1996).
[33] F. D. Kahn, Bull. Astron. Inst. Neth. **12**, 187 (1954).
[34] H. Susa H., 2007, Astrophys. J. **659**, 908 (2007).
[35] H. Susa, Publ. Astron. Soc. Jpn. **58**, 445 (2006).
[36] M. Bate and A. Burkert, Mon. Not. R. Astron. Soc. **288**, 1060 (1997).
[37] J. Wolcott-Green and Z. Haiman, Mon. Not. R. Astron. Soc. **412**, 2603 (2011).
[38] T. Hosokawa, H.W. Yorke, and K. Omukai, Astrophys. J. **721**, 478 (2010).
[39] I. Iliev et al., Mon. Not. R. Astron. Soc. **400**, 1283 (2009).
[40] K. Hasegawa and B. Semelin, Mon. Not. R. Astron. Soc., submitted.
[41] K. Hasegawa and M. Umemura, Mon. Not. R. Astron. Soc. **407**, 2362 (2010).
[42] O. Kessel-Deynet and A. Burkert, Mon. Not. R. Astron. Soc. **315**, 713 (2006).

[43] J. Barnes and P. Hut, Nature **324**, 446 (1986).
[44] N. Y. Gnedin, A. V. Kravtsov, and H-W. Chen, Astrophys. J. **672**, 765 (2008).
[45] J. H. Wise and R. Cen, Astrophys. J. **693**, 984 (2009).
[46] A. O. Razoumov and J. Sommer-Larsen, Astrophys. J. **701**, 1239 (2010).
[47] H. Yajima, J-H. Choi, and K. Nagamine, Mon. Not. R. Astron. Soc. **412**, 411 (2011).
[48] E. R. Fernandez and J. M. Shull, Astrophys. J. **731**, 20 (2011).
[49] M. Fioc and B. Rocca-Volmerange, Astron. Astrophys. **326**, 950 (1997).